Published in final edited form as:
J Biomed Opt. 2008 ; 13(4): 044002. doi:10.1117/1.2966703.

Optimal probe design for breast imaging using near-infrared diffused light

Chen Xu,
University of Connecticut, Department of Electrical and Computer Engineering, Storrs, Connecticut 06269

Baohong Yuan, and
University of Connecticut, Department of Electrical and Computer Engineering, Storrs, Connecticut 06269 and The Catholic University of America, Department of Biomedical Engineering, Washington, DC 20064

Quing Zhu
University of Connecticut, Department of Electrical and Computer Engineering, Storrs, Connecticut 06269

Abstract

Shallow lesions less than 1.5-cm deep are frequently seen in breast patients when they are scanned in reflection geometry. Two boundary conditions are compared for imaging shallow lesions, and a new probe design is introduced. A partial reflection boundary condition is suitable for imaging shallow lesions less than 1.0-cm deep; whereas an absorption boundary condition is desirable for imaging lesions more than 1.5-cm deep. Our new probe design incorporates either a partial reflection boundary or an absorption boundary based on *a priori* knowledge of lesion depth provided by coregistered real-time ultrasound images. An angled source is introduced to further improve the illumination of the region between 1.0- to 1.5-cm depths. Simulation, phantom, and freshly excised mouse tumor experiments demonstrate that targets located at different depths can be uniformly reconstructed. A clinical example is given to demonstrate the utility of this new approach for optimally probing lesions located at different depths.

Keywords

boundary conditions; image reconstruction; diffuse optical tomography; ultrasound

1 Introduction

Diffuse optical tomography (DOT) in the near-infrared range has great potential for noninvasive imaging and monitoring tumor angiogenesis development.[1–10] In breast imaging, DOT implemented in reflection geometry has a significant advantage for probing reduced breast tissue thicknesses as compared with transmission and ring geometries. In reflection geometry, patients are scanned in a supine position and the breasts are generally flat and can be further compressed as conventionally done with pulse-echo ultrasound imaging. These factors allow lesions closer to the chest wall to be imaged. In transmission geometry or ring geometry, breasts are either sandwiched between a pair of source and detector planes or

Address all correspondence to: Quing Zhu, University of Connecticut, Department of Electrical and Computer Engineering, Storrs, Connecticut, 06269; Tel: 869-486-5523; Fax: 860-486-2447; E-mail: zhu@engr.uconn.edu.

surrounded by sources and detectors deployed in a ring or multiple rings. Using these two geometries, lesions close to the chest wall are very difficult to access.

The imaging of lesions less than 1.0- to 1.5-cm deep with DOT in reflection geometry presents a challenge. This is because photons traveling from sources to detectors follow "banana" paths when an absorbing boundary condition is used and therefore probe shallow regions with lower sensitivity.[11–13] As a result, shallower lesions very close to the skin surface are difficult to image with good accuracy unless sources and detectors are located on top of the lesion. This requires that the lesion location is approximately known from other imaging modalities, such ultrasound,[14–17] magnetic resonance imaging,[18,19] or x-ray mammography.[20]

We have developed a dual-modality technique that uses coregistered ultrasound images to guide the optical image reconstruction. Ultrasound images and optical data are acquired simultaneously with a handheld probe in which a commercial ultrasound transducer is centrally located and optical fibers are distributed around the periphery. A dual-zone mesh reconstruction scheme has been developed to improve the inversion.[14] Our dual-modality technique has greatly improved the accuracy of optical image reconstruction and therefore classification between benign and malignant breast lesions.[15,17] Because the ultrasound transducer has to occupy the center region for imaging lesions underneath the probe, the minimal distance of optical source and detector pairs across the centrally located lesions is restricted to approximately 2.5 to 3.0 cm depending on the ultrasound transducer size. This limitation has prohibited the implementation of sources and detectors in the central region.

In a reflective boundary, photon paths follow hemispherical trajectories and shallow lesions can therefore be probed with higher sensitivity.[11–13,21] However, as demonstrated in this paper, a reflection boundary is suitable only for probing lesions at less than 1.0-cm depth; whereas an absorption boundary provides higher sensitivity for imaging lesions deeper than 1.5 cm. To bridge the transition from a reflection boundary to an absorption boundary, a tilted source is introduced to improve the light illumination of the shallower region between 1.0- to 1.5 cm depths. As a result, a uniform imaging reconstruction from the skin surface to the chest wall can be achieved. This hybrid probe design has many applications in DOT imaging when the central region is not accessible due to anatomical limitations.

In Sec. 2, we begin with the review of the Monte Carlo (MC) simulation technique used to demonstrate the effects of absorbing and reflection boundary conditions. We then summarize the theory of two boundary conditions and introduce the modified diffusion equation by including an angled source. The probe design, experimental systems, and the imaging reconstruction scheme are also introduced in Sec. 2. In Sec. 3, the absorption and reflection boundaries are compared using MC simulation and phantom experiments. Errors that result from using extrapolated and partial-current boundaries are assessed. Simulations and phantom experiments using an angled source to improve shallower region illumination are presented. A clinical example is given in this section to demonstrate the utility of the new probe. Section 4 provides a summary and final discussion.

2 Methods

2.1 Monte Carlo Method

The MC method[22] was adopted to simulate the light propagation in a scattering medium and to visualize the absorption distribution inside the medium for two different boundary conditions. Briefly, the turbid medium was modeled as having layers with finite thickness (along the depth, *z* axis) of specified optical properties in each layer. In our simulation, millions of photons were generated at each source location. Each photon was incident at the surface of the turbid medium and was assigned a unity weight *W*, which is analogous to light intensity.

Generally, the photon was incident normally to the surface. When an angled source was introduced, the photon was incident with the specified angle. Each photon went through many steps of absorption and scattering processes. After each step, part of the weight ΔW was absorbed by the medium and the weight of the photon was decreased. The photon was scattered following the Henyey-Greenstein function. The medium anisotropy g was chosen to be 0.9 in this simulation. The Roulette technique was used to terminate the photon when $W \leq W_{th}$, where W_{th} was a threshold value. For each photon, it was either absorbed in the medium, or detected at the reflecting surface, or it exited the transmitting surface. After the migration of one particular photon halted, a new photon was launched into the medium at the source location. The MC simulation was performed in the time domain[23] and the resulting temporal data were Fourier transformed to give frequency domain amplitude and phase shift as a function of distance. In this simulation, the boundary condition can be easily controlled through the refractive indexes of the surface layer and the medium layer. If these two layers had matched refractive indexes then the absorption boundary condition was satisfied. If the refractive indexes of these two layers were mismatched, the possible total internal reflection was considered by calculating the Fresnel reflection coefficient.[24] The Fresnel reflection coefficient was compared with a random number, and the reflectance was decided statistically. Therefore, the reflection boundary condition or partial reflection boundary condition can be simulated.

To evaluate the contributions of different boundary conditions and their effects on image reconstruction of a target, the MC program was extended to include a target embedded inside the medium. The size, position, and optical properties of the target were controlled from an input file. The difference compared with the flat layer only MC simulation was the addition of complex reflection and refraction computation between target and medium interfaces.

2.2 Green's Function Solutions to the Diffusion Equation Under Different Boundary Conditions

The general photon density wave $\Phi(\boldsymbol{r}, t)$ at position $\boldsymbol{r}$ and time t is described by the diffusion equation:[25]

$$\frac{1}{v}\frac{\partial}{\partial t}\Phi(\vec{r},t) - D\nabla^2\Phi(\vec{r},t)+v\mu_a\Phi(\vec{r},t)=S(\vec{r},t), \tag{1}$$

where μ_a is the absorption coefficient and D is the diffusion coefficient of the medium, which is related to the reduced scattering coefficient μ_s' by $D=1/(3\mu_s')$. Here v is the speed of light inside the medium. The source term $S(\boldsymbol{r}, t)$ describes the density of photons generated per second. The Green's function solution to the diffusion equation in frequency domain with the partial current boundary condition ($\Phi=\xi_{ext}\partial\Phi/\partial z$) can be written in the cylindrical coordinates as[13]

$$G^{PC}(\rho,z,z_s)=\frac{1}{4\pi D}\left[\frac{\exp(-kr)}{r}+\frac{\exp(-kr_+)}{r_+}\right.$$
$$\left.-\frac{2}{\xi_{ext}}\int_{-\infty}^{-z_s}dz'\exp\left(\frac{z'+z_s}{\xi_{ext}}\right)\frac{\exp(-kr')}{r'}\right], \tag{2}$$

where k is the wave vector, r is the distance between the light source located at depth z_s and an arbitrary point in the medium, r_+ is the distance between the image source located at depth $-z_s$ and the arbitrary point, r' is the distance from the arbitrary point to other image sources with depth of z', and ξ_{ext} is the extrapolated length on the order of $\mu_s'^{-1}$. All parameters can be found in Ref. [13].

Different boundary conditions can be modeled by taking different values of ξ_{ext}: for a reflection boundary $\xi_{ext} \to \infty$ and for an absorption boundary $\xi_{ext} \to 0$. Generally ξ_{ext} can be expressed as

$$\xi_{ext} = \frac{1+R_{eff}}{1-R_{eff}} \frac{2}{3} z_s,$$

where R_{eff} is the effective reflection coefficient at the boundary of a semi-infinite medium.[12] The line integral in Eq. (2) complicates the calculations. By adopting an approximate boundary condition called the extrapolated boundary condition, Eq. (2) can be approximated as

$$G^{EX}(\rho,z,z_s) = \frac{1}{4\pi D}\left[\frac{\exp(-kr)}{r} - \frac{\exp(-kr'')}{r''}\right]. \quad (3)$$

where r is the same as before, but r'' is the distance from an extrapolated image source to the arbitrary point. The depth of the extrapolated image source is determined by ξ_{ext}, which is a function of the effective reflection coefficient R_{eff}. The accuracy of this approximation will be discussed in Sec. 3.2.

2.3 Analytical Equation of an Angled Source Using an Absorption Boundary

An angled source was introduced to improve the light illumination in the transition region of 1.0- to 1.5-cm depth. The diffusion Eq. (1) with an angled source in frequency domain can be modified as

$$D\nabla^2\Phi(\vec{r},\omega) - \left(\mu_a - j\frac{\omega}{v}\right)\Phi(\vec{r},\omega) = -S_0\delta(\vec{r}-\vec{r}_0)\exp\left(j\frac{\omega}{v}\vec{r}\right), \quad (4)$$

where ω is the modulation frequency, and $\vec{r}0$ is the location of an effective isotropic source, which depends on the angle of the incident light. The solution of the modified diffusion equation is similar to Eq. (3) depending on boundary condition parameter ξ_{ext} and the location of the effective isotropic source.

2.4 Probe Design and Experimental System

A frequency domain system was used in the phantom experiments. The system consists of three wavelengths of 690, 780, and 830 nm modulated at 140 MHz and one photomultiplier tube (PMT) detector. Each wavelength was switched to nine source locations on a probe using 3×1 and 1×9 optical switches, and the PMT detector was translated to eight detection locations connected to optical light guides. The clinical system used an identical source system but 10 parallel PMT detectors.[26] At each detector position, both amplitude and phase of the scattered wave were measured and were used to reconstruct the absorption distributions.

The probe configuration shown in Fig. 1 was used for simulation and experiments. An ultrasound transducer was located at the center to provide target size, shape, and depth information. Figure 1(a) is the photograph of the probe made of black plastic, which provides an absorption boundary. One angled source fiber tilted 55 deg from the incident plane was located next to a source fiber of normal incidence. In the comparison study, either the angled or the normal-incident source was connected to the source output. Thus the total number of sources was the same in each experiment. The probe can also be covered with an aluminum plate to provide a partial reflection boundary and the fitted R_{eff} is 0.6. Figure 1(b) is the photograph when the aluminum cover is used for imaging shallower lesions and will be referred to as a partial reflection boundary in the following text.

2.5 Image Reconstruction

The dual-zone mesh scheme is used for imaging reconstruction.[14] Briefly, the entire imaging volume was divided into the background region and the target region. The background region was divided into a relatively coarse mesh of voxel size 1.0×1.0×1.0 cm^3, and the target region was segmented into a fine mesh of voxel size 0.2×0.2 ×0.5 cm^3. As a result, the total number of voxels with an unknown absorption coefficient was significantly reduced. In addition, the total absorption distribution instead of absorption distribution *per se* was reconstructed, and the total absorption distribution was divided by different voxel sizes of target and background region. Because the absorption changes in background region were generally smaller than the lesion region, the total absorption distribution was maintained on the same order for voxels in both regions and the inversion was well conditioned for convergence. The Born approximation was used to relate the measured perturbation and the medium absorption distribution, and the conjugate gradient method was used for inverse reconstruction.

3 Experimental Results

3.1 Comparison of Absorption and Reflection Boundaries

Figure 2(a) shows the MC simulation of the absorption distribution (*x*-*z* projection) using an absorption boundary. An absorber of 0.5-cm radius was located 0.7-cm deep in the medium. Figure 2(b) shows the absorption distribution of the same target and the background using a reflection boundary of $R_{eff}=1$. Both figures were normalized to the total number of photons and displayed in logarithmic scale. The total absorbed weight at the target region, defined as the summation of the absorbed weight in the target volume, in the absorption and reflection boundary cases was 0.0077 and 0.0505, respectively. About 6.5 times higher absorption was obtained with the reflection boundary and consequently larger perturbation could be expected in the measurements.

Figure 3 shows the normalized perturbation distribution caused by a point absorption target as a function of the target depth for absorption ($R_{eff}=0$) and reflection ($R_{eff}=1$) boundaries. In the calculation, a small target with a diameter of 1 mm was used and the difference of the absorption and reduced scattering coefficients between the target and the background medium were 0.3 and 0 cm^{-1}, respectively. The center of the target was located at the middle between the source and the detector. For each depth, the photon density at the detector position was calculated and subtracted by the background photon density, which was calculated from the absence of the target. The result was further divided by the background photon density, which provided a percentage of the photon density change caused by the absorbing target. To compare the results of different boundary conditions, the percentage of photon density changes in each case was normalized to its maximum value. Two typical separation distances of 3 and 7 cm between the source and the detector were adopted. When the reflection boundary was used, the perturbation reached a maximum close to the boundary and reduced as the depth increased. When an absorption boundary was chosen, the maximum perturbation occurred at certain depth depending on the source-detector separation. These results suggest that a reflection boundary should be used for detecting shallow targets and an absorption boundary for deeper lesions.

3.2 Comparison of Extrapolated Boundary and Partial-Current Boundary

As discussed in Sec. 2.2, an effective reflective coefficient R_{eff} was introduced to account for partial reflection of photons from a boundary. For the thin aluminum plate used, the best fitted R_{eff} is 0.6. It has been known that the extrapolated boundary condition fails when R_{eff} is close to unity. [12,13] To evaluate the validity of the extrapolated boundary approximation when $R_{eff}=0.6$, we numerically calculated the error of photon distribution caused by an absorbing target from Eqs.(2) and (3), respectively. Figure 4(a) shows the amplitude error and 4(b) shows the phase error between the extrapolated and partial-current boundary conditions. The

amplitude errors were about 1.26%, 1.58%, and 2.09% for typical source-detector pairs separated by 3, 4, and 6 cm, respectively, when R_{eff} =0.6. Correspondingly, the phase errors were −1.34, −0.82, and −0.47 deg, respectively. It is obvious that when R_{eff} =0.6, the extrapolated boundary condition is very close to the partial-current boundary condition.

3.3 Phantom Experiment Using Reflection and Absorption Boundaries

To validate the simulations, a set of phantom experiments was performed using the system described in Sec. 2.4. An Intralipid (Baxter, Deerfield, Illinois) solution was used to emulate typical breast tissue optical properties of μ_a =0.03 cm^{-1} and μ_s'=6.3 cm^{-1}. The high-contrast target was a 1.0-cm diameter sphere made of polyester resin of calibrated values μ_a =0.23 cm^{-1} and μ_s'=5.45 cm^{-1} at 780 nm. The low-contrast target had the same size, but different optical properties of μ_a =0.07 cm^{-1} and μ_s'=5.50 cm^{-1} calibrated at the same wavelength. The data were collected separately using the black probe [Fig. 1(a)] with no angled source and the probe with the aluminum cover [Fig. 1(b)] when each target was located at 0.7, 1.0, and 1.5 cm in depth, respectively. The left and right columns of Fig. 5 show the reconstructed images using both boundary conditions at 780 nm. The color bar represents the reconstructed absorption coefficient. The left column [Figs. 5(a), 5(d), and 5(g)] shows the reconstructed images obtained from the black probe; the right column [Figs. 5(c), 5(f), and 5(i)] displays images obtained from the probe with the aluminum cover. The middle column [Figs. 5(b), 5 (e), and 5(h)] shows the reconstructed images using the probe shown in Fig. 1(a) with one angled source, which will be compared in the later section. The reconstructed maximum values and the mean values within full width at half maximum (FWHM) are given in Table 1 (first and third columns). At a shallower depth of 0.7 cm, the reconstructed target μ_a value and shape have been improved when the aluminum cover was used. When the depth was increased to 1 cm, the reconstructed target μ_a obtained from the black probe with the angled source was more accurate than that of using the black probe only and the aluminum cover. The μ_a obtained from the aluminum-covered probe was better than the black probe only. At the 1.5-cm depth, the best result regarding to reconstructed target μ_a was obtained from the black probe with absorbing boundary condition.

Similar experiments were performed for the low-contrast target and the reconstruction results are shown in Fig. 6 for both boundary conditions at 780 nm. The reconstructed maximum and mean values are given in Table 2 (first and third columns). The middle column shows the results obtained from the black probe with the angled source. For the low-contrast target, the shape of the reconstructed image using the absorption boundary is better than the partial reflection boundary at 1- and 1.5-cm depth, however, the image at 0.7-cm depth is distorted. The reconstructed image at 0.7-cm depth is improved under the partial reflection boundary condition. When the average target μ_a was used to compare three configurations, the black probe with the angled source provided a more accurate target μ_a at 1-cm depth and the black probe with no-angled source was the best at 1.5-cm depth.

To further validate the phantom experiments, we have performed one set of mouse tumor experiments. The excised tumor was heterogeneous with three lobular structures and was placed inside a transparent cuvette of 1 cm in size. The cuvette was located at 1.0- and 1.6-cm depths within an Intralipid solution of fitted optical properties μ_a =0.023 cm^{-1} and μ_s'=7.0 cm^{-1} at 780 nm. For each target depth, two sets of data were acquired by using two probes: an absorbing probe without angled source [Fig. 1(a)] and the probe with aluminum cover [Fig. 1(b)]. Reference data were acquired using the corresponding probe. The absorption map obtained with the aluminum cover at 1-cm depth [see Fig. 7(b)] showed higher μ_a of maximum 0.122 cm^{-1} and improved target shape compared with the absorption map obtained at the same depth using the black absorbing probe [see Fig. 7(a)]. The reconstructed maximum

μ_a obtained with the black probe was 0.088 cm^{-1}. At 1.6-cm depth, the absorption map obtained with the black probe demonstrated a higher reconstructed μ_a of maximum 0.137 cm^{-1} [see Fig. 7(c)] and improved target definition compared with the map obtained with the aluminum cover [see Fig. 7(d)]. The reconstructed maximum μ_a obtained with the aluminum cover was 0.101 cm^{-1}. Thus, more uniform reconstruction can be achieved with the use of partial reflection boundary for a shallower depth, such as 1 cm, and an absorbing boundary at depths beyond 1.0 cm. This set of results agrees with phantom experiments shown in Fig. 5.

3.4 Simulation Results with Angled Source

Using the MC method, the forward data using sources with normal incidence and one angled source, referred to as the angled probe, were generated from the probe configuration shown in Fig. 1(a). The reconstructed images for the 1.0-cm diameter target are shown in Fig. 8 along with values for the simulation parameters. Figure 8(a) is the reconstructed image using the probe with sources at normal incidence, and Fig. 8(b) is the reconstructed image using the angled probe. The total number of sources used in obtaining the images [1(a)] and [1(b)] is the same. For both images, the first slice is the spatial *x*-*y* image of 6 cm×6 cm obtained at 0.2 cm, and the second slice is at the depth of 0.7 cm with 0.5-cm spacing between slices. In Fig. 8(a), the image is blurred and shifted from the center position. The maximum reconstructed value is μ_a =0.162 cm^{-1}, which is about 54% of the true value, and the mean is 0.122 cm^{-1}, which is 41% of the true value. In Fig. 8(b), both the reconstructed value and location of the target are improved compared with Fig. 8(a). The maximum reconstructed value in Fig. 8(b) is μ_a =0.270 cm^{-1}, which is about 90% of the true value, and the mean is 0.196 cm^{-1}, which is about 65% of the true value. These results demonstrate that tilted sources may further improve the shallow region illumination. The experimental implementation of tilted sources, however, presents a limitation for clinical studies [see Sec. 4].

Simulations of different target contrast were performed to evaluate the probe with one angled source. In the simulations, the background properties were kept as μ_a =0.03 cm^{-1} and μ_s'=6.0 cm^{-1} while the target μ_a varied from 0.1 to 0.3 cm^{-1} in 0.1 cm^{-1} increments. The target was μ_s' kept as 6.0 cm^{-1}. The spherical target of 1-cm diameter was located at (0, 0, 0.7 cm). Figure 9 plots the reconstructed maximum values (dashed line) and the mean values (dotted line) with different probes. The blue solid line shows the true values. The black dashed line is the reconstructed maximum value from the angled probe with normal-incident sources and one angled source, and the black dotted line is the reconstructed mean value from this probe. The red dashed line is the reconstructed maximum value obtained from the probe with all normal-incident sources, and the red dotted line is the reconstructed mean value. The reconstructed values at low contrast region are close for both probes. For higher contrasts, the performance of the angled probe is superior to that with all normal-incident sources.

3.5 Phantom Experiments Using the Angled Probe

Phantom experiments were performed to validate the results obtained from the simulations. An Intralipid solution of optical properties μ_a =0.03 cm^{-1} and μ_s'=6.3 cm^{-1} was used. The high- and low-contrast targets were the same as used before. The data were collected using the probe shown in Fig. 1(a) with the angled source connected to the source fiber when the target was positioned at 0.7-, 1.0-, and 1.5-cm depths. Figures 5(b), 5(e), and 5(h) show the reconstructed images obtained from the high-contrast target. For the target located at 0.7-cm depth, the angled probe improved the reconstruction accuracy by 16% compared with the probe of all normal-incident sources. At this target depth, the best result in terms of reconstruction accuracy was obtained from the probe with the aluminum cover [Fig. 5(c)]. Figure 5(e) is the reconstructed image when the target is located at 1.0-cm depth. For the high-contrast target, the probe with all normal-incident sources can reconstruct the image at the correct location, but the maximum

reconstructed μ_a value is 0.149 cm^{-1} (65% of true value). The angled probe provides a similar result, but the reconstructed μ_a value is 0.180 cm^{-1} (78% of true value), which is better than the probe with the aluminum cover for which the reconstructed value was 0.163 cm^{-1} (71% of true value). It is clear that the angled probe can provide better target shape and improved reconstructed value compared with the probe with all normal-incident sources, especially in the range of 0.7 to 1.0 cm. At 1.5-cm depth, the results obtained from the angled probe and the probe with normal-incident sources are comparable. For the high-contrast target at this depth, the maximum reconstructed μ_a value obtained from the probe with normal-incident sources is 0.204 cm^{-1}, which is 89% of the true value, and the maximum μ_a value of the angled probe is 0.20 cm^{-1}, which is 87% of the true value. The reconstructed maximum values and means within FWHM are listed in the second column of Table 1. For the low-contrast target, as we expected, both probes provided similar results. The reconstructed maximum values and means are listed in the second column of Table 2. It is clear that the tilted source in the angled probe increased the detection sensitivity to shallow targets located at approximately 1-cm depth and improved the reconstruction results compared with the probe will all normal-incident sources.

3.6 A Clinical Example

An example was obtained from our ongoing clinical study conducted at the University of Connecticut Health Center. The study protocol was approved by the local Institutional Review Board and the informed consent was obtained from the patient. The black angled probe without and with aluminum cover of absorption and partial reflection boundary condition [see Fig. 1] was used to evaluate a 6-mm lesion of a 53-year-old patient prior to her ultrasound-guided core biopsy. Figures 10(a) and 10(d) show the coregistered ultrasound images of the 6-mm lesion located at 1-cm depth when the black angled probe with and without the aluminum cover were used, respectively. The corresponding absorption maps obtained at 780 nm as well as the computed total hemoglobin maps without and with the aluminum cover are shown in Figs. 10 (b) and 10(c) and Figs. 10(e) and 10(f3, respectively. The maximum and mean lesion μ_a at 780 nm were 0.144 and 0.098 cm^{-1} for the angled probe and 0.088 and 0.064 cm^{-1} for the aluminum probe. The computed total hemoglobin maximum and mean were 62.0 and 44.3 μM/l for the angled probe and 53.1 and 38.4 μM/l for the aluminum probe, respectively. Based on the comparison studies shown in Figs. 5(e) and 5(f) and Fig. 6(e) and 6(f) (see Tables 1 and 2), the mean values of the angled probe are more accurate than the aluminum probe at this target depth. Ultrasound-guided core biopsy revealed a benign fibroadenoma. The total hemoglobin levels obtained agree with the benign findings reported by us earlier.[15,17]

4 Discussion and Summary

The ability to accurately image shallow lesions less than 1.0-to 1.5-cm deep with DOT in reflection geometry is important because 10% to 30% of patients have lesions in this range. The absorption and reflection boundaries have certain sensitivity ranges and can be best combined to optimally probe lesions located at different depths as demonstrated in this paper. The angled sources can further improve the light illumination in this shallower region and work synergistically with the two boundary conditions to provide more uniform reconstruction across the target depths from surface to 1.0- to 1.5-cm depths.

The optimal boundary condition or probe selection was evaluated using simulations, phantoms, and an excised tumor. For clinical studies, the background tissue absorption and scattering have a wide range and the transition depth between the sensitivity ranges of the two boundary conditions may change accordingly. A more robust transition depth relationship accounting for differing bulk tissue optical properties remains to be validated by more clinical cases.

The tilt angle and the number of tilted sources in our design were based on simulation results and experimental considerations. Figure 11 shows simulation results of maximum

reconstructed μ_a versus source angle tilted from normal incidence. The forward data were generated using the MC simulation from the probe shown in Fig. 1(a). The other experiment conditions were the same as those documented in Sec. 3.4. The angled source was tilted at 0 (normal incidence), 30, 45, 60, and 65 deg. The reconstructed maximum μ_a were 0.162 (54%), 0.181 (60.3%), 0.213 (71.0%), 0.270 (90.0%), and 0.279 cm^{-1} (93.0%), respectively. From simulation, the angled source tilted at 65 deg from the normal incident was needed to significantly improve the reconstruction accuracy. However, this angle was difficult to implement on the plastic probe with about 1-cm thickness and therefore a 55-deg angle was used in the experiments. Simulations also show that three angled sources can improve the quantification accuracy of the high-contrast target up to 95% at the depth of 0.7 cm; whereas one tilted source at center can reconstruct about 90% of the true value. However, the number of available normal-incident sources will be reduced when probing deeper lesions. Therefore, only one tilted source was deployed on the probe.

In Ref. 26, we have introduced the use of different modulation frequencies to probe lesions located at different depths. The high-modulation frequency in the range of 350 MHz or higher can improve the detection sensitivity of shallower lesions; however, the system hardware design is more complex due to factors such as higher signal losses of circuit components, PMT frequency response, and noise. The phase unwrapping is also a difficult task due to the rapid change of phase profile received from all source-detection separations. The probe design introduced in this paper is much easier to implement. The selection of an appropriate probe in a clinical setting is as simple as choosing different transducers in routine ultrasound examinations. Currently, we are using this new probe in our ongoing clinical studies.

We have shown that a handheld probe that can flexibly incorporate either a partial reflection boundary or an absorption boundary can significantly improve the reconstruction accuracy of targets located at different depths. An angled source can further improve the illumination of the shallow region between 1.0- to 1.5-cm depths. Simulations, phantom experiments, an excised mouse tumor, and a clinical example have demonstrated the synergistic utility of this new approach.

Acknowledgements

The authors appreciate the funding support of this work from National Institutes of Health (Grant No. R01EB002136), the Patrick & Catherine Weldon Donaghue Medical Research Foundation, and ARMY Medical Research and Materiel Command Predoctoral Training award (No. 81XWH-05-1-0299). The authors thank graduate student Diego Castillo for helping with the probe construction and Dr. John Gamelin for reviewing the manuscript.

References

1. Yodh A, Chance B. Spectroscopy and imaging with diffusing light. Phys Today 1995;48(3):34–40.
2. Tromberg B, Shah N, Lanning R, Cerussi A, Espinoza J, Pham T, Svaasand L, Butler J. Non-invasive *in vivo* characterization of breast tumors using photon migration spectroscopy. Neoplasia 2000;2(12): 26–40. [PubMed: 10933066]
3. Chance B, Nioka S, Zhang J, Conant E, Hwang E, Briest S, Orel S, Schnall M, Czerniecki B. Breast cancer detection based on incremental biochemical and physiological properties of breast cancers: a six-year, two-site study. Acad Radiol 2005;12(8):925–933. [PubMed: 16023383]
4. Poplack S, Tosteson T, Wells W, Pogue B, Meaney P, Hartov A, Kogel C, Soho S, Gibson J, Paulsen K. Electromagnetic breast imaging: results of a pilot study in women with abnormal mammograms. Radiology 2007;243(2):350–359. [PubMed: 17400760]
5. Grosenick D, Moesta K, Wabnitz H, Mucke J, Stroszczynski C, Macdonald R, Schlg P, Rinneberg H. Time-domain optical mammography: initial clinical results on detection and characterization of breast tumors. Appl Opt 2003;42(16):3170–3186. [PubMed: 12790468]

6. Spinelli L, Torricelli A, Pifferi A, Taroni P, Danesini G, Cubeddu R. Characterization of female breast lesions from multi-wavelength time-resolved optical mammography. Phys Med Biol 2005;50(11): 2489–2502. [PubMed: 15901950]
7. Choe R, Corlu A, Lee K, Durduran T, Konecky S, Grosicka-Koptyra M, Arridge S, Czerniecki B, Fraker D, DeMichele A, Chance B, Rosen M, Yodh A. Diffuse optical tomography of breast cancer during neoadjuvant chemotherapy: a case study with comparison to MRI. Med Phys 2005;32(4):1128–1139. [PubMed: 15895597]
8. Heffer E, Pera V, Schutz O, Siebold H, Fantini S. Near-infrared imaging of the human breast: complementing hemoglobin concentration maps with oxygenation images. J Biomed Opt 2004;9(6): 1152–1160. [PubMed: 15568935]
9. Gu X, Zhang Q, Bartlett M, Schutz L, Fajardo L, Jiang H. Differentiation of cysts from solid tumors in the breast with diffuse optical tomography. Acad Radiol 2004;11(1):53–60. [PubMed: 14746402]
10. Schmitz C, Klemer D, Hardin R, Katz M, Pei Y, Graber H, Levin M, Levina R, Franco N, Solomon W, Barbour R. Design and implementation of dynamic near-infrared optical tomographic imaging instrumentation for simultaneous dual-breast measurements. Appl Opt 2005;44(11):2140–2153. [PubMed: 15835360]
11. Feng S, Zeng F, Chance B. Photon migration in the presence of a single defect: a perturbation analysis. Appl Opt 1995;34(19):3826–3837.
12. Haskell R, Svaasand L, Tsay T, Feng T, McAdams M, Tromberg B. Boundary conditions for the diffusion equation in radiative transfer. J Opt Soc Am A 1994;11(10):2727–2741.
13. Passchens JCJ, Hooft GW'T. Influence of boundaries on the imaging of objects in turbid media. J Opt Soc Am A 1998;15(7):1797–1812.
14. Zhu Q, Chen N, Kurtzman S. Imaging tumor angiogenesis by the use of combined near infrared diffusive light and ultrasound. Opt Lett 2003;28(5):337–339. [PubMed: 12659436]
15. Zhu Q, Huang M, Chen NG, Zarfos K, Jagjivan B, Kane M, Hegde P, Kurtzman S. Ultrasound-guided optical tomographic imaging of malignant and benign breast lesions. Neoplasia 2003;5(5):379–388. [PubMed: 14670175]
16. Zhu Q. Optical tomography with ultrasound localization: initial clinical results and technical challenges. Technol Cancer Res Treat 2005;4(3):235–244. [PubMed: 15896078]
17. Zhu Q, Cronin EB, Currier AA, Vine HS, Huang M, Chen N, Xu C. Benign versus malignant breast masses: optical differentiation with US-guided optical imaging reconstruction. Radiology 2005;237 (1):57–66. [PubMed: 16183924]
18. Ntziachristos V, Yodh A, Schnall M, Chance B. Concurrent MRI and diffuse optical tomography of breast after indocyanine green enhancement. Proc Natl Acad Sci USA 2000;97(6):2767–2772. [PubMed: 10706610]
19. Brooksby B, Pogue B, Jiang S, Dehghani H, Srinivasan S, Kogel C, Tosteson TD, Weaver J, Poplack SP, Paulsen KD. Imaging breast adipose and fibroglandular tissue molecular signatures by using hybrid MRI-guided near-infrared spectral tomography. Proc Natl Acad Sci USA 2006;103(23):8828–8883. [PubMed: 16731633]
20. Li A, Miller E, Kilmer M, Brukilacchio T, Chaves T, Scott J, Zhang Q, Wu T, Chorlton M, Moore R, Kopans D, Boas D. Tomographic optical breast imaging guided by three-dimensional mammography. Appl Opt 2003;42(25):5181–5190. [PubMed: 12962399]
21. Yuan B, Zhu Q. Ultrasound-guided diffuse optical tomography of shallow target with reflection boundary. Proc SPIE 2005;5693:265–270.
22. Wang L, Jacques SL, Zheng L. MCML-Monte Carlo modeling of light transport in multi-layered tissues. Comput Methods Programs Biomed 1995;47:131–146. [PubMed: 7587160]
23. Das M, Xu C, Zhu Q. Analytical solution for light propagation in a two-layer tissue structure with a tilted interface for breast imaging. Appl Opt 2006;45(20):5027–5036. [PubMed: 16807614]
24. Hecht, E. Optics. 2. Addison-Wesley; Boston: 1987.
25. Ishimaru, A. Wave Propogation and Scattering in Random Media. Academic; New York: 1978.
26. Zhu Q, Xu C, Guo P, Aquirre A, Yuan B, Huang F, Castilo D, Gamelin J, Tannenbaum S, Kane M, Hedge P, Kurtzman S. Optimal probing of optical contrast of breast lesions of different size located at different depths by US localization. Technol Cancer Res Treat 2006;5(4):365–380. [PubMed: 16866567]

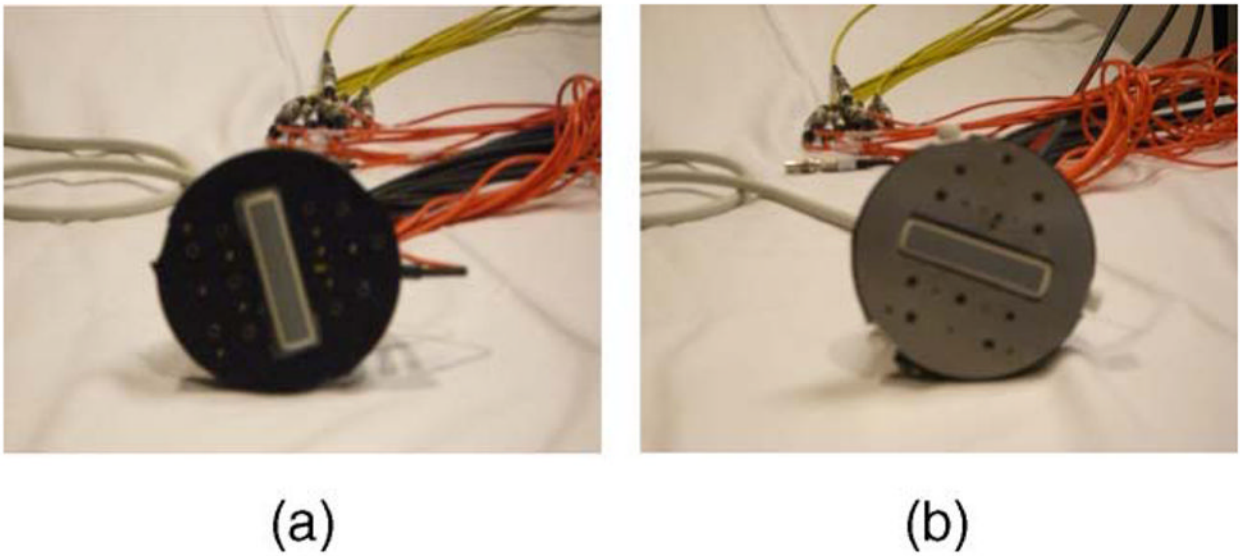

Fig. 1.
Photograph of the new probe that incorporates an absorption boundary with an angled source (a) or a partial reflection boundary using an aluminum cover (b). The ultrasound probe was located at the center and the optical source and detector fibers were distributed at the periphery of the ultrasound probe.

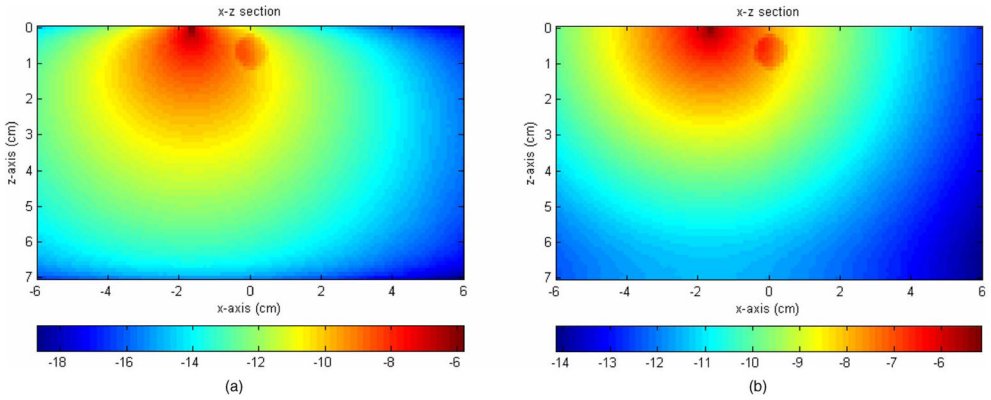

Fig. 2.

Logarithmic scale display of absorption distributions inside the medium computed using an absorption boundary (a) and a reflection boundary (b). The medium has dimensions of 12×12×7 cm^3. The figure was displayed as *x*-*z* projection; *x* axis is the lateral dimension and *z* is the depth. The medium background optical properties were $\mu_a = 0.03^{-1}$ and $\mu_s' = 6.0\ cm^{-1}$; the target optical properties were $\mu_a = 0.3\ cm^{-1}$ and $\mu_s' = 6.0\ cm^{-1}$. The target was a 0.5-cm radius sphere located at (0, 0, 0.7 cm), and the source was located at (−1.7 cm, 0, 0).

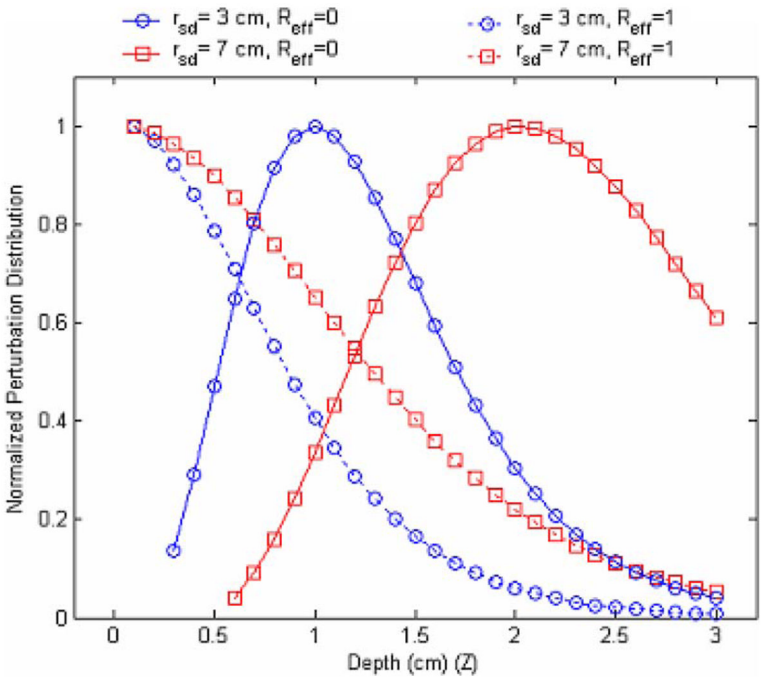

Fig. 3.

Perturbation distribution as a function of the target depth for an absorption boundary (R_{eff} =0) and reflection boundary (R_{eff} =1). Two typical source-detector distances of 3 and 7 cm were selected.

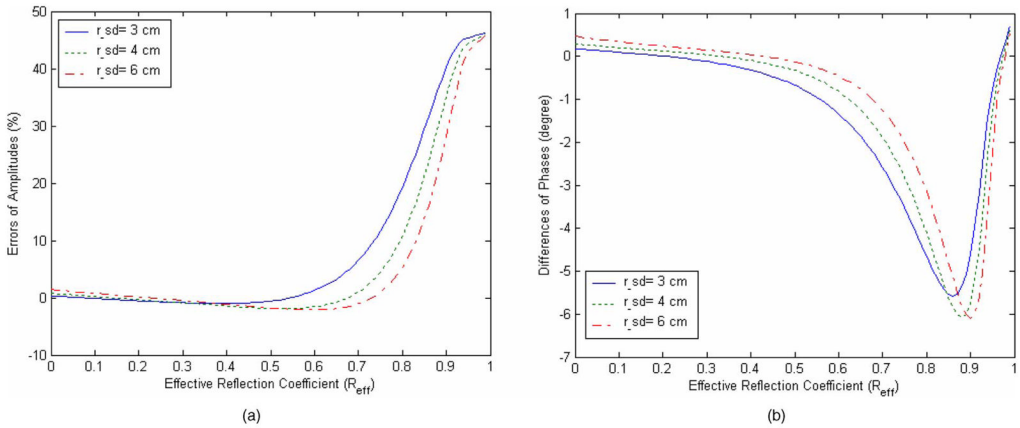

Fig. 4.

Errors between two boundary conditions as a function of effective reflection coefficient. Three typical source-detector distances of 3, 4, and 6 cm were shown in figures. (a) Relative errors of amplitude. (b) Phase errors.

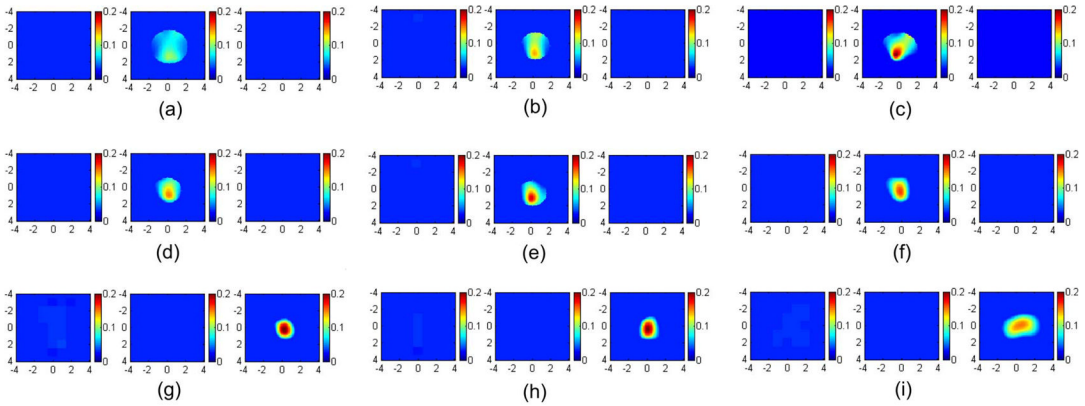

Fig. 5.

Images of the high-contrast absorber reconstructed from different boundary conditions. The left column was obtained using the absorption boundary; the middle column was obtained using the absorption boundary with one angled source; the right column was obtained using the partial reflection boundary. In (a), (b), and (c), the target center was located at 0.7-cm depth. The first slice is the spatial *x*-*y* image of 8 cm×8 cm obtained at 0.2-cm depth, and the second and third cross-sections slice at 0.7- and 1.2-cm depths. In (d), (e), and (f), the target center was located at 1.0-cm depth. The first slice is obtained at 0.5 cm and the second and third at 1.0- and 1.5-cm depths. In (g), (h), and (i), the target center was located at 1.5-cm depth. The reconstructed maximum and mean values were shown in Table 1.

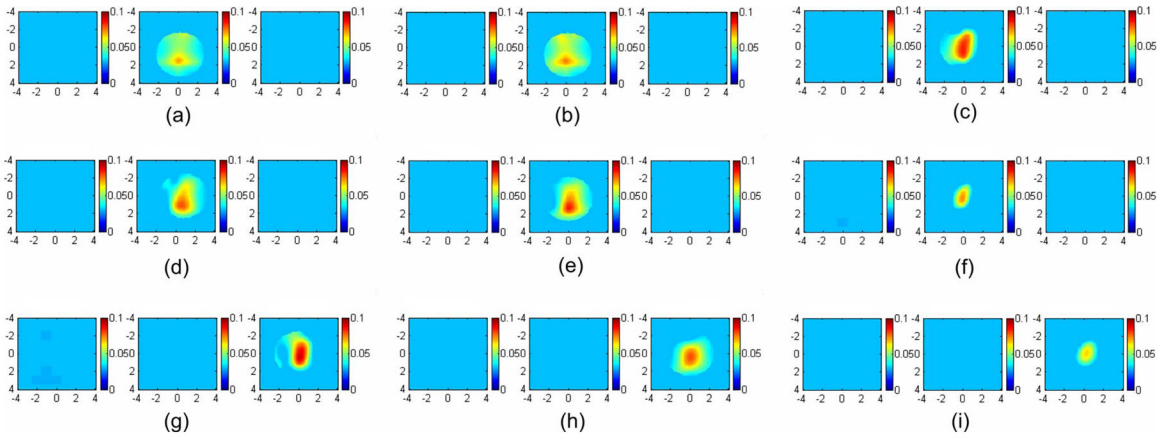

Fig. 6.

Images of the low-contrast absorber reconstructed from different boundary conditions. The left column was obtained using the absorbing boundary; the middle column using the absorption boundary with one angled source; the right column using the partial reflection boundary condition. In (a), (b), and (c), the target center was located at 0.7-cm depth. In (d), (e), and (f), the target center was located at 1.0-cm depth. In (g), (h), and (i), the target center was 1.5-cm depth. The reconstructed maximum and mean values were shown in Table 2.

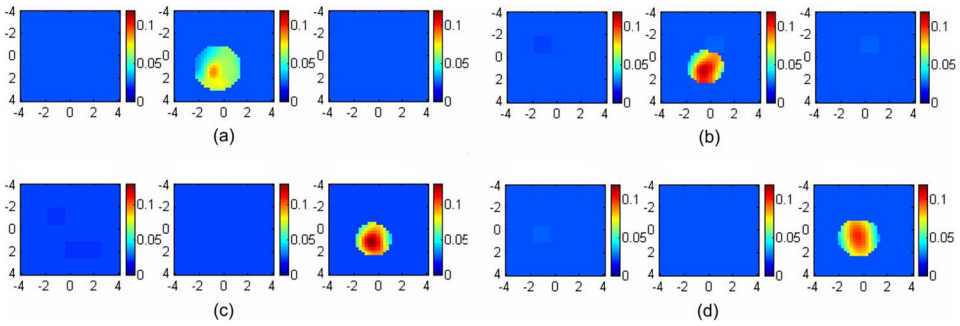

Fig. 7.

Images of an excised mouse tumor reconstructed from different boundary conditions. The left column [(a) and (c)] was obtained using the absorbing boundary; the right column [(b) and (d)] using the aluminum cover. In (a) and (b), the tumor center was located at 1.0-cm depth. The reconstructed maximums were 0.088 and 0.122 cm^{-1}, respectively. In (c) and (d), the tumor center was located at 1.6-cm depth. The reconstructed maximums were 0.137 and 0.101 cm^{-1}, respectively.

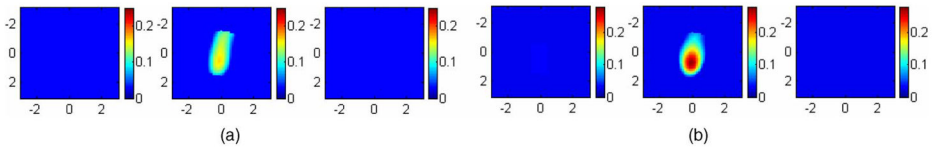

Fig. 8.

The reconstructed image for a simulated target using the black probe with normal-incident sources (a) and the angled probe (b). The background optical properties of the medium were μ_a =0.03 cm^{-1} and μ_s'=6.0 cm^{-1}. The target was located at the center (0, 0, 0.7 cm) with radius 0.5 cm and μ_a =0.3 cm^{-1} and μ_s'=6.0 cm^{-1}. For both images, the first slice is the spatial *x*-*y* image of 6 cm×6 cm obtained at 0.2 cm, and the second slice is at the depth of 0.7 cm with 0.5-cm spacing between slices. In (a), the maximum reconstructed value was μ_a =0.162 cm^{-1} (54% of the true value), and in (b), the maximum μ_a =0.27 cm^{-1} (90%).

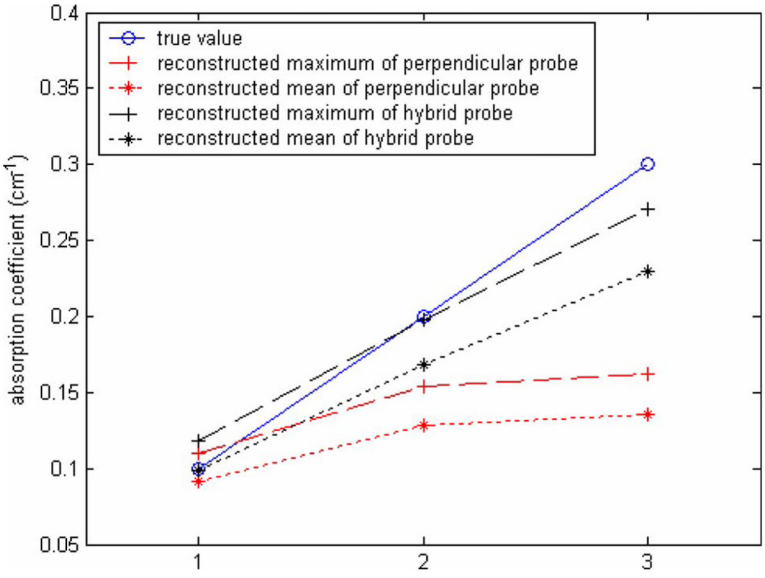

Fig. 9.

Reconstruction results for a 1-cm diameter spherical target at (0, 0, 0.7 cm) from the probe with all normal-incident sources and the angled probe with normal-incident sources and one angled source.

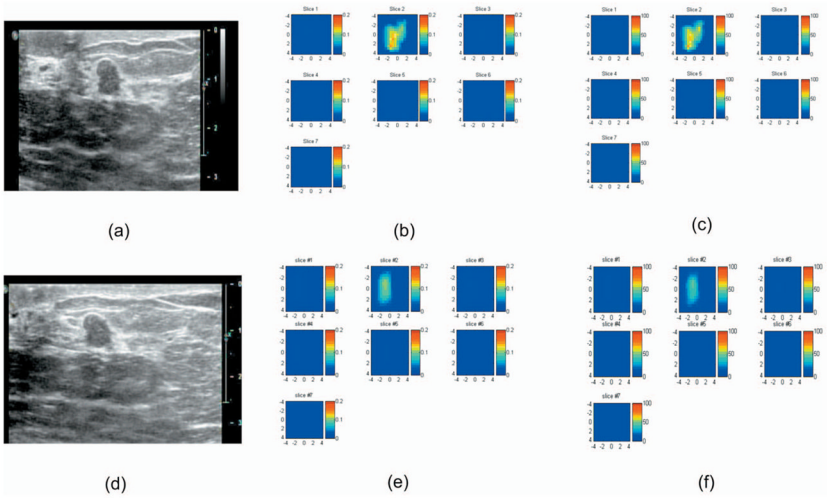

Fig. 10.

(a) Coregistered ultrasound image, (b) the corresponding absorption map obtained at 780 nm, and (c) total hemoglobin map obtained from 53-year-old woman using the black angled probe shown in Fig. 1(a). (d) Coregistered ultrasound image, (e) the corresponding absorption map obtained at 780 nm, and (f) total hemoglobin map using the same probe with the aluminum cover. In absorption and total hemoglobin maps, each slice corresponds to a spatial image of 9 cm×9 cm obtained at 0.3 cm underneath the skin surface to 3.3 cm deep toward the chest wall with 0.5-cm spacing in depth. The fitted background absorption and reduced scattering coefficients from the normal side of the breast were 0.01, 3.78 cm^{-1} (780 nm), and 0.012, 4.23 cm^{-1} (830 nm), respectively. The core biopsy result revealed a benign fibroadenoma.

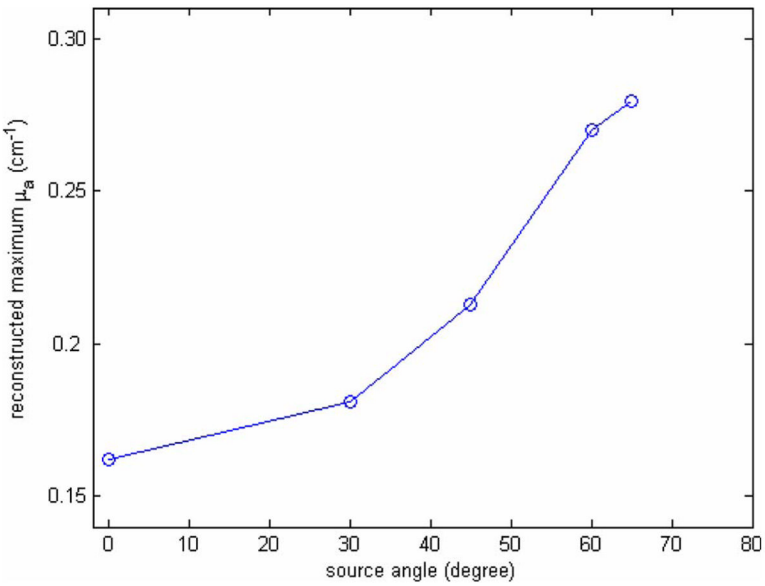

Fig. 11.

The reconstructed maximum μ_a when the source has different tilted angle. The background optical properties of the medium were μ_a =0.03 cm^{-1} and μ_s'=6.0 cm^{-1}. The target was located at the center (0, 0, 0.7 cm) with radius 0.5 cm and μ_a =0.3 cm^{-1} and μ_s'=6.0 cm^{-1}.

Table 1

The reconstructed maximum values and mean values of the high-contrast target (μ_a =0.23 cm^{-1}) under different conditions at 780 nm.

	Normal-Incident Sources with Absorption Boundary		Normal-Incident Sources and One Angled Source Using Absorption Boundary		Normal-Incident Sources with Partial Reflection Boundary	
Depth (cm)	**Max (cm^{-1})**	**Mean (cm^{-1})**	**Max (cm^{-1})**	**Mean (cm^{-1})**	**Max (cm^{-1})**	**Mean (cm^{-1})**
0.7	0.107 (46%)	0.086 (37%)	0.141 (61%)	0.113 (49%)	0.200 (87%)	0.166 (72%)
1.0	0.149 (65%)3	0.124 (54%)	0.180 (78%)	0.150 (65%)	0.163 (71%)	0.138 (60%)
1.5	0.204 (89%)	0.174 (76%)	0.200 (87%)	0.169 (74%)	0.150 (65%)	0.128 (55%)

Table 2

The reconstructed maximum values and mean values of the low-contrast target (μ_a =0.07 cm^{-1}) under different conditions at 780 nm.

	Normal-Incident Sources with Absorption Boundary		Normal-Incident Sources and One Angled Source Using Absorption Boundary		Normal-Incident Sources with Partial Reflection Boundary	
Depth (cm)	**Max (cm^{-1})**	**Mean (cm^{-1})**	**Max (cm^{-1})**	**Mean (cm^{-1})**	**Max (cm^{-1})**	**Mean (cm^{-1})**
0.7	0.071 (101%)	0.055 (79%)3	0.075 (106%)	0.059 (84%)	0.085 (121%)	0.072 (103%)
1.0	0.079 (113%)	0.067 (95%)	0.085 (121%)	0.069 (99%)	0.073 (104%)	0.062 (89%)
1.5	0.091 (130%)	0.077 (110%)	0.079 (113%)	0.067 (95%)	0.065 (92%)	0.054 (77%)